Influence of finite-size and edge effects on the exchange-bias properties of ferromagnetic/antiferromagnetic nanodots: Granular Monte Carlo investigation

Haydar Kanso, Renaud Patte, Vincent Baltz, Denis Ledue

Influence of finite-size and edge effects on the exchange-bias properties of ferromagnetic/antiferromagnetic nanodots: Granular Monte Carlo investigation

Haydar Kanso,[1,*] Renaud Patte,[1] Vincent Baltz,[2] and Denis Ledue[1,†]
[1]*Normandie Université, UNIROUEN, INSA Rouen, CNRS, GPM, F-76800 Saint Étienne du Rouvray, France*
[2]*Université Grenoble Alpes, CNRS, CEA, Grenoble INP, INAC-Spintec, F-38000 Grenoble, France*

(Received 5 October 2018; revised manuscript received 14 December 2018; published 11 February 2019)

In this paper, we investigate exchange-biased square nanodots whose lateral sizes range between 130 and 500 nm, in comparison with continuous films by kinetic Monte Carlo simulations. We use a granular model which takes into account disordered interfacial phases by considering less stable magnetic grains at the interface in the antiferromagnetic (AF) layer. We further model the effect of the nanofabrication process by considering grains with reduced surfaces at the edges, due to grain cutting. Since less stable grains at the nanodot edges in the AF layer have been experimentally evidenced, we assumed a weaker anisotropy for the grains which are in the AF layer at the dot edges. Our results evidence two different mechanisms of the ferromagnetic (F) layer reversal depending on the magnitude of the coupling between F grains. In the weak coupling regime relative to the anisotropy, the exchange field is independent of the coupling and no variability from one nanodot to another is observed. By contrast, in the strong coupling regime, the exchange field depends on the coupling and it shows a high variability from one nanodot to another. Our model also well explain some experimental features observed in NiFe/IrMn nanodots (for various lateral sizes) and continuous films, at various measurement temperatures and various AF thicknesses. Finally, our model explains a long lasting issue about why the exchange field in nanodots can be either smaller or larger than in continuous films.

DOI: 10.1103/PhysRevB.99.054410

I. INTRODUCTION

Exchange-bias (EB) effect occurs due to the exchange coupling at the interface between F and AF materials [1–4], leading to a shift of the hysteresis loop which is known as the EB field (H_E). EB, mainly in F/AF bilayers, has been extensively investigated in the last few decades, from both experimental and theoretical points of view. In terms of technological applications, exchange-biased bilayers constitute an essential part of spin valves and magnetic tunnel junctions used in the field of spintronics [5,6]. More recently, the challenge becomes increasing the magnetic storage density and the miniaturization of devices (magnetic sensors, high-density data storage media) [7]. For that, it is crucial to extend the investigations of the EB mechanism to nanostructures [8]. In the case of exchange-biased bilayers, it is of particular interest to study how EB properties are modified when passing from a continuous F/AF film to nanodot arrays (with a lateral size of a few hundred nanometers). Indeed, EB properties depend on various parameters such as bulk anisotropies, bulk and interfacial exchange couplings, and grain volumes in polycrystalline films. Such a phenomenon becomes more complicated at the nanoscale, due to edge and finite-size effects which well affect EB properties compared to continuous films. Actually, contradictory results on H_E have been reported. For example, in NiFe/IrMn bilayers, it was found that H_E at room temperature is smaller in nanodots for thicknesses $t_{\mathrm{IrMn}} < 11$ nm and larger above this thickness [9,10]. In a more recent investigation on NiFe/IrMn nanodots (t_{IrMn} 7–8 nm) [11], it was observed that H_E, at room temperature, is smaller when the size decreases, while at 10 K it is larger with decreasing the size. Also, in NiFe/FeMn square dots ($t_{\mathrm{FeMn}} = 10$ nm), it was shown that H_E at room temperature decreases with the size decrease [12] in agreement with Refs. [9–11]. In contrast, it was observed that H_E at room temperature is smaller in NiFe/IrMn nanodots with $t_{\mathrm{IrMn}} = 15$ nm [13] in contradiction with Refs. [9–11]. In another recent study on Co/IrMn square nanodots [14], it was reported that the dot lateral size has no significant effect on H_E at room temperature ($3\,\mathrm{nm} < t_{\mathrm{IrMn}} < 15\,\mathrm{nm}$). It should be noted that H_E versus t_{IrMn} exhibits a maximum at $t_{\mathrm{IrMn}} = 6.5$ nm for all dot sizes. In Co/CoO nanostructures, for small Co thickness ($t_{\mathrm{Co}} = 8$ nm) a strong increase in H_E at 4 K was detected as the lateral size decreases [15]. However, at large Co thickness ($t_{\mathrm{Co}} = 25$ nm), the increase of H_E is less pronounced. One possible explanation of the difference between nanodots and continuous films is the dot edges which induce additional locations for the formation of spin-glass-like AF regions [16]. So, according to the data previously mentioned, it seems that H_E measured at room temperature decreases as the dot size decreases (at least for small AF thicknesses) while it is the opposite at low temperatures. However, these results depend on several conditions such as the AF layer thickness, the initial annealing temperature, and the lateral size of bilayers.

At the same time, there are only a few numerical studies of EB properties in F/AF nanodots. They are divided into two categories: those based on an atomistic model and others based on a granular one. An atomistic model assuming a

*haydar.kanso@etu.univ-rouen.fr
†denis.ledue@univ-rouen.fr

small fraction of spins pinned ferromagnetically in the AF interface plane has been developed [17]. This study, based on Monte Carlo simulations, showed an increase of H_E of patterned systems compared to a continuous film. Concerning the granular approach, a significant difference in H_E between nanodots and continuous films has been reported [18]. However, such a granular model is rather simple since it does not take into account disordered interfacial phases (spin-glass-like regions) in the AF layer which are usually considered [11,19,20]. These interfacial phases can significantly affect the EB properties. In particular, at working temperatures for devices, they contribute to device-to-device variability of EB once the film is nanofabricated [21].

In this study, we investigate EB properties of square F/AF nanodots using a granular model which includes less stable magnetic regions at the F/AF interface [22,23]. In addition, due to the nanofabrication process, less stable grains at the nanodot edges in the AF layer are considered as experimentally demonstrated [16]. We first investigate the effect of the coupling between F grains on the variability of H_E from one nanodot to another and on the F layer magnetization reversal mechanism. Then we study EB properties at room temperature of nanodots in comparison with continuous films for various AF thicknesses. Moreover, we investigate the nanodot size effects on the temperature dependence of H_E. In these two cases, our results are successfully compared to recent experimental data on NiFe/IrMn bilayers. Our investigations are performed using kinetic Monte Carlo simulations.

The remainder of the paper is organized as follows. The model and simulation technique are described in Sec. II. Numerical results and discussions are given in Sec. III. A conclusion is given in Sec. IV.

II. MODEL AND SIMULATION

In order to simulate EB properties of F/AF bilayers, we generate a system of two layers with a F layer of thickness t_F and an AF layer of thickness t_{AF}. Since columnar growth is assumed, the two layers have the same granular microstructure which is generated by Voronoi tessellation in two dimensions [24]. To model disordered interfacial phases [11,19,20], small grains (SG) of thickness $t_{SG} < t_{AF}$ are randomly distributed over the F/AF interface within the AF layer [22,23]. Such disordered interfacial phases are produced by magnetic frustration which is induced by the defects at the F/AF interface (e.g., interlayer diffusion and stacking faults). So, we assume that these SG exhibit altered magnetic properties compared to those of the AF bulk. It worth noting that a difference between nanodots and continuous films is the small number of grains (few hundreds) in nanodots due to their reduced lateral sizes. In addition, to be close to real nanodots, we model the effect of the nanofabrication process by the presence of grains with reduced surfaces at the edges due to grain cutting [Fig. 1(a)]. Moreover, we assume that those grains which are located in the AF layer have the same altered magnetic properties as the SG [Fig. 1(b)] [16]. To ease the discussion, these grains located at the edges in the AF layer will be referred as SG_E. It should be noted that $t_{SG_E} = t_{AF}$ is larger than t_{SG} [see Fig. 1(b)]. Consequently, the blocking temperature T_B distribution within a given nanodot might differ from that of a

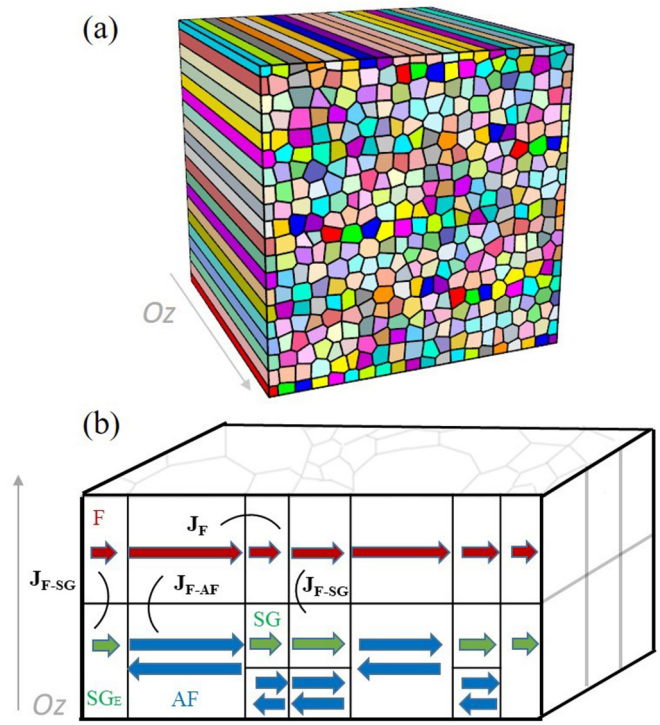

FIG. 1. (a) Top view of the granular microstructure of a nanodot with grains of reduced surfaces at the edges. (b) Sketch of the F/AF nanodot with SG randomly spread over the F/AF interface in the AF layer and SG_E at the edges in the AF layer (in green).

continuous film. Since the dimensions of the grains are in the nanometer scale, each grain is considered as a single magnetic domain that reverses by uniform rotation. Thus, a unit vector $\boldsymbol{\sigma}_i$ represents the magnetization orientation of each F grain, each SG, each SG_E, and the interfacial uncompensated magnetization orientation of each bulk AF grain. At the interface, each F grain is coupled with an AF grain (J_{F-AF}), or an SG, or—in the case of nanodots—an SG_E (J_{F-SG}) [Fig. 1(b)]. In agreement with the literature, the AF grains are decoupled from each other [25–27], as well as from the SG and SG_E grains. In contrast, the F grains are coupled to each other (J_F) [Fig. 1(b)]. Uniaxial anisotropy along a common easy axis (y axis) in the plane of the layer is considered for all grains, and a linear thermal dependence of the anisotropy constants per unit volume K_i is implemented [28]. Thus, the total energy of the system can be expressed as

$$E = -\sum_{\langle i,j \rangle} J_{ij}\boldsymbol{\sigma}_i \cdot \boldsymbol{\sigma}_j - \sum_i K_i V_i (\boldsymbol{\sigma}_i \cdot \boldsymbol{e}_y)^2 - \mu_0 \mathbf{H} \cdot \sum_{i \in F,SG,SG_E} \mathbf{m}_i, \quad (1)$$

where V_i is the grain volume, $\mathbf{m}_i$ is the magnetic moment of a F grain or a SG or a SG_E (in the nanodots), and $\mathbf{H}$ is the magnetic field applied along the y axis.

Most parameters of our model can be either found in literature or reasonably estimated from experimental data. The effective interfacial coupling per unit area, j_{F-AF}, can be deduced from the maximum value of H_E in the case of an ideal F/AF interface, i.e., without SG, nor SG_E. Taking into account

TABLE I. Fixed parameters of all our simulations.

$j_{F-AF}(Jm^{-2})$	$T_N(K)$	$K^0_{AF}(Jm^{-3})$	$K^0_{SG}(Jm^{-3})$	$t_{SG}(nm)$	$x_{SG}(\%)$
1.5×10^{-4}	690	4×10^5	3×10^5	2	50

TABLE II. Summary of parameter values used in Sec. III A.

$t_F = 12\,nm$	$t_{AF} = 5\,nm$
$4 \times 10^{-5} \leqslant j_F\,(Jm^{-2}) \leqslant 4 \times 10^{-4}$	$j_{F-SG} = 8.5 \times 10^{-5}\,Jm^{-2}$
$T_M = 4\,K$ (or 298 K)	$T_0 = 550\,K$

the maximum value of $|H_E|$ measured in Ref. [10] for $t_{IrMn} = 9\,nm$, we found that $j_{F-AF} = 1.5 \times 10^{-4}\,Jm^{-2}$ is a reasonable value for NiFe/IrMn bilayers. The 0-K anisotropy constant for AF grains is taken to be $K^0_{AF} = 4 \times 10^5\,Jm^{-3}$ [29]. The Néel temperature of the AF layer used in the expression of its anisotropy constant [28,30] is $T_N = 690\,K$ [3]. By contrast, the coupling per unit area, j_{F-SG}, and the effective anisotropy of SG and SG_E are unknown. We assume that j_{F-SG} is smaller or equal to j_{F-AF}. Similarly the effective anisotropy of SG and SG_E is assumed to be weaker than that of the AF grains to report on the lower blocking temperatures of the disordered interfacial and dot edge phases demonstrated experimentally [16]. From a theoretical point of view, this can be justified because the noncollinearity of the spins in these phases should induce a decrease of the effective anisotropy constant. We arbitrarily set $K^0_{SG} = 0.75K^0_{AF}$. We point out that when K^0_{SG} increases, the blocking temperatures of SG and SG_E increase which results in a shift toward larger temperatures of the low temperature part of the H_E vs T_a (see Sec. III B 1) or T_M (see Sec. III B 2) curves. The fixed parameters of all our simulations are summarized in Table I. Note that the other parameters j_F, j_{F-SG}, t_F, and t_{AF} are given in each section.

Based on experimental measurements [31,32], disordered interfacial phases extend over 3–4 atomic planes, thus we set $t_{SG} = 2\,nm$. In fact, it was demonstrated experimentally that the fraction of SG x_{SG} may be varied between about 20% and 80%, as it is sensitive to interfaces and concomitant layers intermixing, and that it therefore depends on the stack and fabrication process [33]. For that in our simulations, we fixed the fraction of SG x_{SG} at the interface to an average value of 50% in both nanodots and continuous films. Let us mention that an increase of x_{SG} results in a small decrease of the exchange field at the temperatures above the maximum blocking temperature of the SG. Note that, in the case of nanodots, there is an additional contribution of grains with altered magnetic properties due to SG_E (the fraction of SG and SG_E is 58% on average for $L = 130\,nm$).

The simulations are performed in such a way as to reproduce experimental procedures [10,11]. First, in order to study the variability between nanodots in Sec. III A and to compare H_E in nanodots with that in continuous films in Sec. III B 1, we simulate by the kinetic Monte Carlo method [34,35] the Soeya protocol [36]. This protocol consists of a first initial field cooling (FC) under a positive field H_{FC} from T_0 down to $T_M = 4\,K$ (or 298 K). Then successive annealings up to higher temperatures T_a such that $T_M \leqslant T_a < T_0$ followed by a FC under a negative field down to T_M are performed. This step is realized to gradually reorient the entities in contact with the F layer which satisfy $T_B < T_a$. Hysteresis loops are collected at T_M after each increment of T_a. Thus, T_a is the variable parameter during the process. Second, to study size effect in Sec. III B 2, we use another procedure which consists of a unique FC under a positive field H_{FC} from T_0 down to 5 K. Then, successive hysteresis loops are measured at increasing temperatures T_M ($T_M \geqslant 5\,K$). Details of Monte Carlo simulations are given in Refs. [22,30].

It is worth noting that three regimes of grains in the AF layer in contact with the F layer should be differentiated according to their T_B. Grains with $T_B > T_0$ are not polarized by the field-cooling process; they remain randomly oriented with zero net magnetization and consequently do not contribute to H_E in average. Grains with $T_B < T_M$ are polarized but are superparamagnetic at T_M, thus their contribution to H_E is null. Hence, only the grains with $T_M < T_B < T_0$ contribute to H_E.

III. RESULTS AND DISCUSSIONS

A. Effect of F grains coupling

In this part, we investigate the effect of the effective coupling per unit area between the F grains j_F on H_E measured at T_M versus the annealing temperature (T_a) for NiFe (12 nm)/IrMn (5 nm) nanodots and continuous films. To do so, we simulate the Soeya protocol mentioned in Sec. II from $T_0 = 550\,K$ down to $T_M = 4\,K$ (or 298 K). Within our simulations, the size of nanodots is $L = 130\,nm$, which corresponds to 289 grains per layer. The coupling between the F grains and SG is set to $j_{F-SG} = 8.5 \times 10^{-5}\,Jm^{-2}$. The parameter values are summarized in Table II.

Our results clearly show that there exist two different regimes depending on whether j_F is weak or strong compared to $2K_F l_F/z_F$ where l_F is the lateral dimension of the grain and z_F is the number of interacting F grains. As mentioned above, since H_E is directly related to T_B of the grains in the AF layer (AF grains, SG and SG_E in case of nanodots) in contact with the F layer, we plot the distribution of the intrinsic T_B (T_B in the absence of coupling and applied field) [23] of these entities in Fig. 2. We can see that since $T_0 = 550\,K$ is larger than the maximum value of T_B, all the grains in contact with the F layer are polarized during the initial FC and can contribute to H_E depending on T_M.

1. Measurement temperature $T_M = 4\,K$

According to Fig. 2, all the grains which are in contact with the F layer are blocked at $T_M = 4\,K$, so that all of these grains contribute to H_E. We first investigate the effect of j_F on the variability of H_E from one nanodot to another. The T_a dependencies of H_E for several nanodots with $j_F = 4 \times 10^{-4}\,Jm^{-2}$ (strong coupling since $2\,K_F\,l_F/z_F = 6.5 \times 10^{-5}$ for $z_F = 4$) and $4 \times 10^{-5}\,Jm^{-2}$ (weak coupling) are plotted in Fig. 3. The variability is significant when $j_F = 4 \times 10^{-4}\,Jm^{-2}$ whereas it decreases as j_F decreases (not shown) and vanishes for $j_F = 4 \times 10^{-5}\,Jm^{-2}$. The T_a dependence of H_E (averaged over 60 nanodots) is shown in Fig. 4 for $4 \times 10^{-5}\,Jm^{-2} < j_F < 4 \times 10^{-4}\,Jm^{-2}$. We checked that averaging over a larger number of nanodots does not change the results.

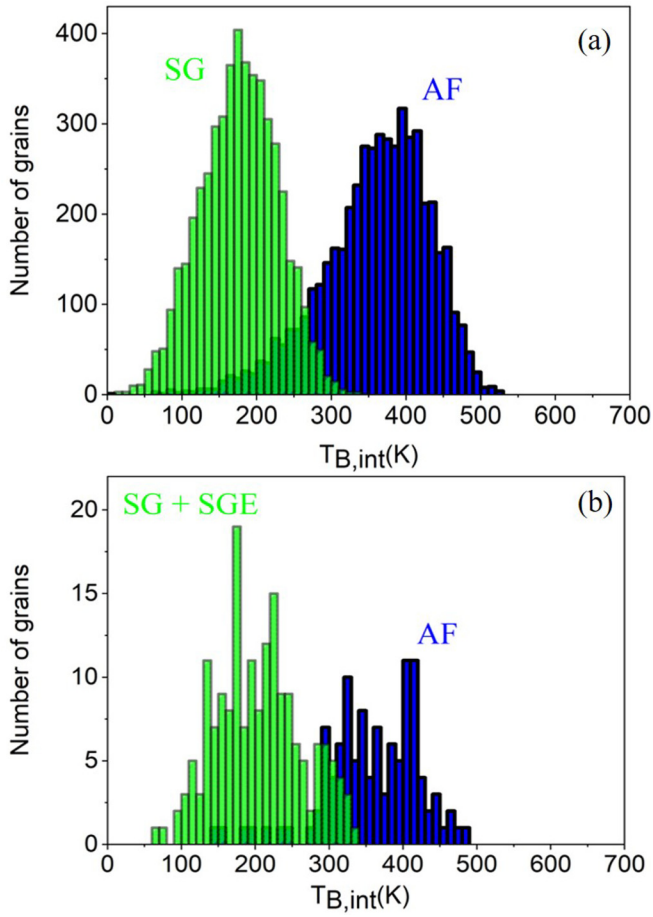

FIG. 2. Intrinsic blocking temperature distributions for the grains in the AF layer which are in contact with the F layer at the interface calculated from the volume distribution for (a) a continuous film (AF grains and SG) and (b) a nanodot with $L = 130$ nm (AF grains, SG, and SG_E) in NiFe/IrMn(5 nm) bilayers (the AF grains are in blue and the SG and SG_E are in green).

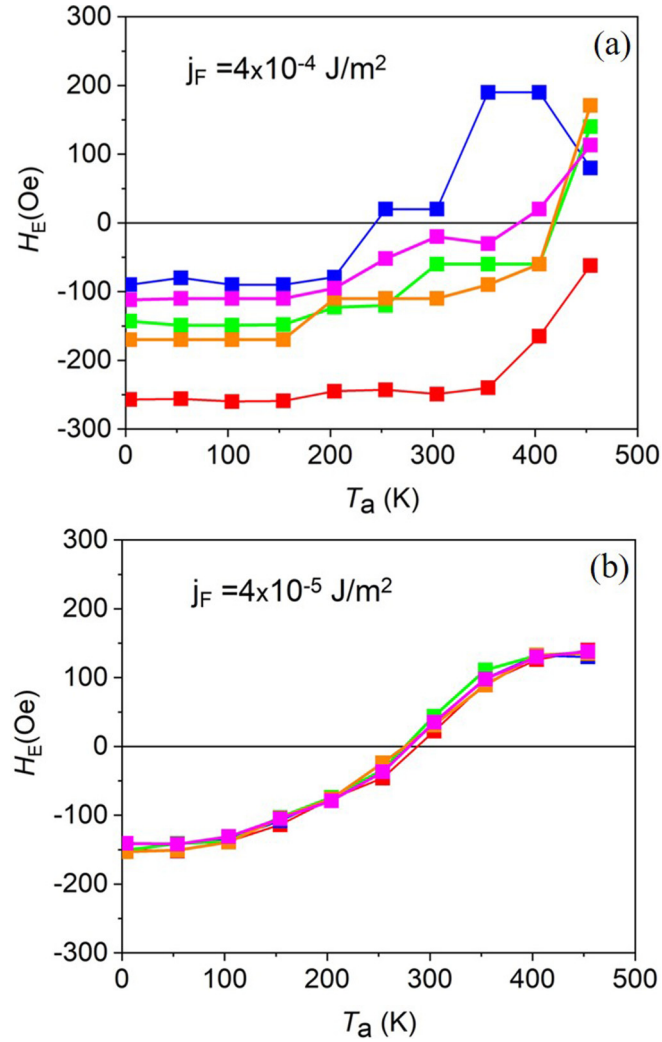

FIG. 3. T_a dependence of H_E measured at $T_M = 4$ K for (a) 5 NiFe(12 nm)/IrMn(5 nm) nanodots ($L = 130$ nm) with $j_F = 4 \times 10^{-4}$ Jm^{-2}, and (b) $j_F = 4 \times 10^{-5}$ Jm^{-2}.

We note that such an averaging is equivalent, experimentally, to make magneto-optical Kerr (MOKE) effect measurements on an array of nanodots with a laser spot size much larger than the pitch of the array [9,11], or to perform magnetometry measurement on a full array. In contrast, data for isolated nanodots can be obtained experimentally either by MOKE when the size of the laser spot is smaller than the pitch of the array, or most likely through electrical measurements where each nanodot is contacted electrically, like in magnetic random access memories [21]. We compare our results with the expression of H_E assuming that the F layer behaves as a macrospin coupled to the AF one with an average interfacial coupling $\langle j_{int} \rangle$:

$$H_E = \frac{\langle j_{int} \rangle}{\mu_0 M_F t_F}, \tag{2}$$

where M_F is the magnetization of each F grain and $\langle j_{int} \rangle$ is expressed as

$$\langle j_{int} \rangle = \tfrac{1}{2}[(1-2r) j_{F-AF} + (1-2r') j_{F-SG}], \tag{3}$$

where r is the fraction of AF grains in contact with the F layer negatively repolarized, and r' is the fraction of SG and SG_E negatively repolarized (these fractions increase with T_a) [23]. It is important to note that within this assumption, H_E does not depend on j_F. From Fig. 4, it can be seen that our simulated values of H_E coincide with the average-coupling behavior given by Eq. (2) only if j_F is small enough (here $j_F = 4 \times 10^{-5}$ Jm^{-2}). Thus our data clearly evidence two different regimes: an average-coupling behavior with no variability as j_F is weak enough and a j_F dependent behavior with high variability when j_F increases. It is also seen that the j_F dependence is more pronounced for higher T_a. For a better understanding, the effect of j_F on the F layer reversal mechanism is shown in Fig. 5. We can see that for $j_F = 4 \times 10^{-4}$ Jm^{-2}, the F layer reversal starts with a grain located at one of the corners of the nanodot [red grain in Fig. 5(a)]. This grain acts as a nucleation center because it has a lower energy barrier due to a lack of F neighbors and its small volume. Then due to the large value of j_F, the magnetization reversal of the F layer propagates from this corner. So, the forward and backward reversal fields depend on the neighbors of the nucleation center (AF, SG, SG_E) and on the number of F neighbors.

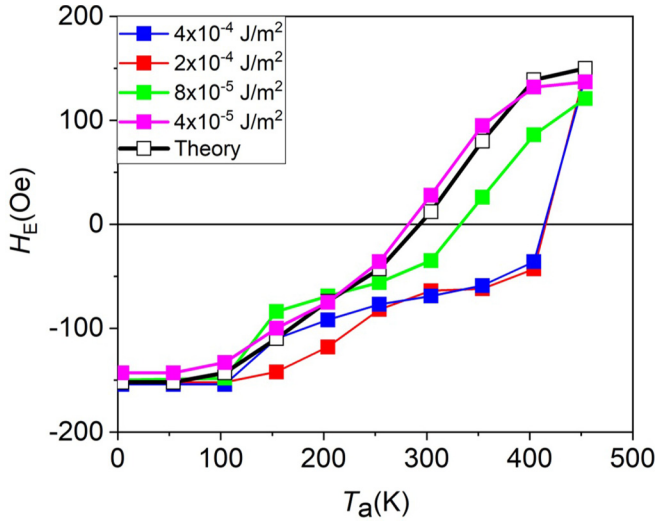

FIG. 4. T_a dependence of H_E measured at $T_M = 4$ K averaged over 60 NiFe(12 nm)/IrMn(5 nm) nanodots ($L = 130$ nm) for 4×10^{-5} Jm^{-2} $< j_F <$ 4×10^{-4} Jm^{-2}.

This environment differs between one nanodot and another leading to the observed variability in H_E. Such a variability actually agrees with earlier experimental results reported in [21]. On the contrary, for $j_F = 4 \times 10^{-5}$ Jm^{-2}, the reversal starts at different places [several nucleation centers, red grains of Fig. 5(b)] without propagation. Then F/AF coupling is averaged over these nucleation centers and H_E is proportional to the average coupling $\langle j_{int} \rangle$. Thus the consequence is the absence of variability in that case which is desirable from a technological point of view. Finally, we can conclude that the average-coupling behavior (weak j_F) is associated with a reversal with several nucleation centers without propagation, while the j_F dependent behavior (strong j_F) corresponds to a reversal with a propagation from a single nucleation center.

2. *Measurement temperature* $T_M = 298$ K

For $T_M = 298$ K, only the grains in the AF layer which are in contact with the F layer at the interface, and having 298 K $< T_B <$ 550 K, contribute to H_E. From Fig. 2, we can see that a large fraction of AF grains contribute to H_E, whereas

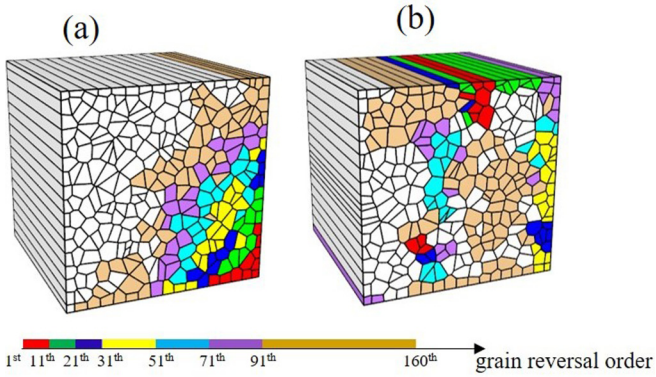

FIG. 5. F grain reversal sequence at $T_M = 4$ K for (a) $j_F = 4 \times 10^{-4}$ Jm^{-2} and (b) $j_F = 4 \times 10^{-5}$ Jm^{-2} in NiFe(12 nm)/IrMn(5 nm) nanodots with $L = 130$ nm.

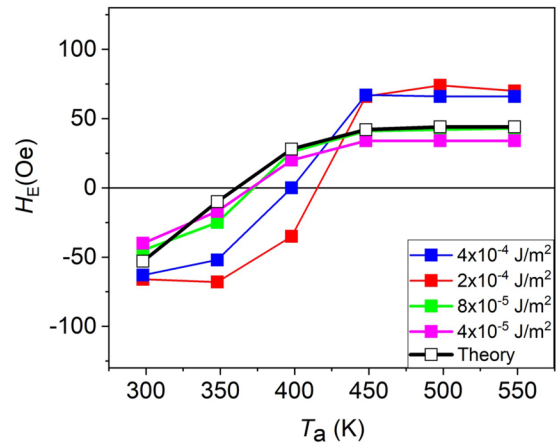

FIG. 6. T_a dependence of H_E measured at $T_M = 298$ K averaged over 60 NiFe(12 nm)/IrMn(5 nm) nanodots ($L = 130$ nm) for 4×10^{-5} Jm^{-2} $< j_F <$ 4×10^{-4} Jm^{-2}.

SG and SG$_E$ do not contribute. Similar to $T_M = 4$ K, we observe that the variability from one nanodot to another decreases as j_F decreases and vanishes for $j_F = 4 \times 10^{-5}$ Jm^{-2} (not shown here). The T_a dependence of H_E (averaged over 60 nanodots) for 4×10^{-5} Jm^{-2} $< j_F <$ 4×10^{-4} Jm^{-2} is given in Fig. 6. Again, we compare our simulated values with the average-coupling behavior [Eq. (2)] where

$$\langle j_{int} \rangle \approx \frac{(1-2r)}{2} j_{F-AF}. \quad (4)$$

As for $T_M = 4$ K, we find that the average-coupling behavior is satisfied if j_F is weak enough. Note that for $j_F = 4 \times 10^{-4}$ Jm^{-2}, the F layer reversal does not start necessarily with a grain located at one corner of the nanodot unlike the case $T_M = 4$ K due to thermal agitation (not shown here).

B. Comparison with experimental data

In this section, we investigate NiFe/IrMn bilayers and we compare our results to experimental data [10,11] in order to propose an explanation for the difference between the nanodot behavior and the continuous film behavior. Experimental findings [9,11] report MOKE measurements on arrays of nanodots with a laser spot size much larger than the pitch of the array. A spot of about 1-mm diameter for an array pitch of around 200 nm and a total array area of 1×1 mm^2 was used in Ref. [9], and complete 100×100 μm^2 arrays of square dots with several lateral sizes 300 (interdot distance 100), 500 (interdot distance 300), and 1000 (interdot distance 300) nm were probed in Ref. [11]. As a consequence, the experimental data that were obtained correspond to an average over numerous nanodots. We therefore averaged our results over several nanodots where we found that 60 nanodots of averaging is enough for convergence. We took $j_F = 4 \times 10^{-5}$ Jm^{-2} and $j_{F-SG} = 1.5 \times 10^{-4}$ Jm^{-2}.

1. *NiFe/IrMn bilayers* ($T_M = 298$ K)

Here we investigate the T_a dependence of H_E for various t_{IrMn} with $t_{NiFe} = 12$ nm. The simulation procedure is the same as in Sec. II (Soeya protocol) with an initial FC under

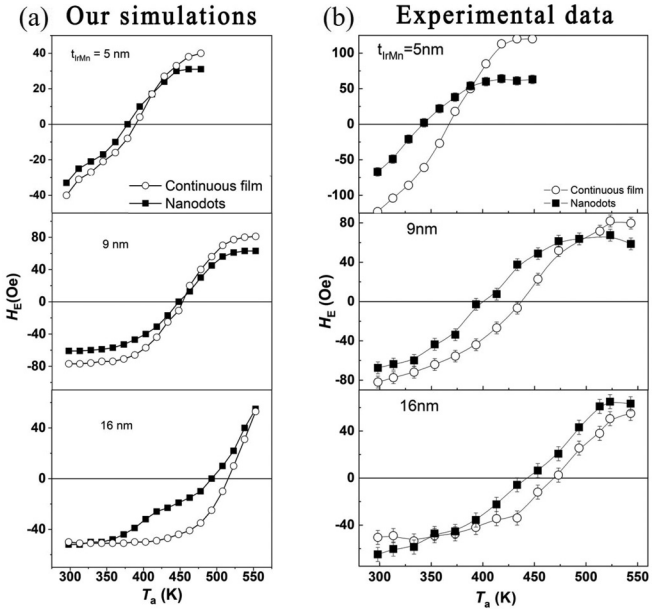

FIG. 7. Simulated T_a dependence of H_E measured at $T_M = 298$ K for (a) NiFe/IrMn bilayers ($t_{IrMn} = 5$, 9, and 16 nm), compared to experimental data [10] (b).

$H_{FC} = 2.4$ kOe from $T_0 = 550$ K down to $T_M = 298$ K. In Fig. 7(a), we show the simulated T_a dependence of H_E for $t_{IrMn} = 5$, 9 and 16 nm. The parameter values are summarized in Table III. A shift of the H_E curve to higher temperatures as t_{IrMn} increases is observed which is in good qualitative agreement with experimental observations [Fig. 7(b)] [10]. We can explain these results as follows: (i) Here, the main contribution to H_E is due to the AF grains (those with 298 K $<$ T_B $<$ 550 K), the SG do not contribute, and the SG_E give a small contribution only for the nanodot with $t_{IrMn} = 16$ nm; (ii) then the derivative dH_E/dT_a is proportional to the T_B distribution of the AF grains contributing to H_E [22,23]; (iii) consequently, since the T_B distribution of the AF grains shifts to higher temperatures as t_{IrMn} increases the curve of the derivative and thus the H_E curve versus T_a shifts towards higher value of T_a as t_{IrMn} increases. In agreement with experimental data, the simulated value of $|H_E|$ at $T_a = 298$ K is smaller in nanodots for $t_{IrMn} = 5$ nm and 9 nm which can be explained by the presence of SG_E in nanodots which do not contribute to H_E for these thicknesses. On the contrary, $|H_E|$ at $T_a = 298$ K is slightly larger in nanodots for $t_{IrMn} = 16$ nm in qualitative agreement with the experimental data. These results come from the contribution of SG_E since their T_B (which increases with t_{IrMn}) is in the window delimited by 550 K and 298 K for this AF thickness. We insist on the fact

TABLE III. Summary of parameter values used in Sec. III B 1.

$t_F = 12$ nm	$t_{AF} = 5$, 9, and 16 nm
$j_F = 4 \times 10^{-5}$ Jm^{-2}	$j_{F-SG} = 1.5 \times 10^{-4}$ Jm^{-2}
$T_M = 298$ K	$T_0 = 550$ K

TABLE IV. Summary of parameter values used in III B 2.

$t_F = 8$ nm	$t_{AF} = 8$ nm
$j_F = 4 \times 10^{-5}$ Jm^{-2}	$j_{F-SG} = 1.5 \times 10^{-4}$ Jm^{-2}
$5 \leqslant T_M$ (K) $\leqslant 300$	$T_0 = 300$ K

that all the parameters except t_{IrMn} were kept the same for the six simulated curves given in Fig. 7(a).

2. NiFe/IrMn bilayers (T_M = variable)

Our aim here is to investigate the lateral size effects on the temperature dependence of H_E in NiFe/IrMn systems with $t_{NiFe} = t_{IrMn} = 8$ nm in comparison with Ref. [11]. The procedure consists of a unique FC under $H_{FC} = 500$ Oe from $T_0 = 300$ K down to 5 K. Then, successive hysteresis loops are measured at increasing temperatures $T_M \geqslant 5$ K. The parameter values are summarized in Table IV. The simulated temperature dependence of $|H_E|$ is shown in Fig. 8(a). Again, a good qualitative agreement with the experimental data in Fig. 8(b) is obtained: $|H_E|$ is larger in small nanodots at 5 K whereas it is the opposite as the temperature increases (for T_M around 150–200 K). The reason is that at $T_M = 5$ K, in both systems, only a small fraction of AF grains (those with 5 K $<$ T_B $<$ 300 K since $T_0 = 300$ K) and all SG contribute to H_E. But in the case of nanodots, there is an additional contribution due to SG_E. Consequently, $|H_E|$ is larger in nanodots. Since the fraction of SG_E decreases as the size increases, $|H_E|$ decreases when the size increases. As T_M increases, the fraction of SG and SG_E that contribute to H_E decreases which explains the decrease in $|H_E|$. For T_M $>$ 150 K, $|H_E|$ becomes larger in continuous films because there are more SG polarized towards the positive orientation of the field, thus the positive reversal field becomes smaller in continuous films. Note that we observe a difference between the simulated values of $|H_E|$ and the experimental ones because we choose the value of j_{F-AF} to fit the maximum value of $|H_E|$ for $t_{IrMn} = 9$ nm of Ref. [10]. However, the present experimental data have been obtained in two different laboratories on distinct samples. So the quality of the F/AF interface is likely not the same due to the differences in the fabrication process, i.e., the effective interfacial F-AF coupling in the present samples is larger.

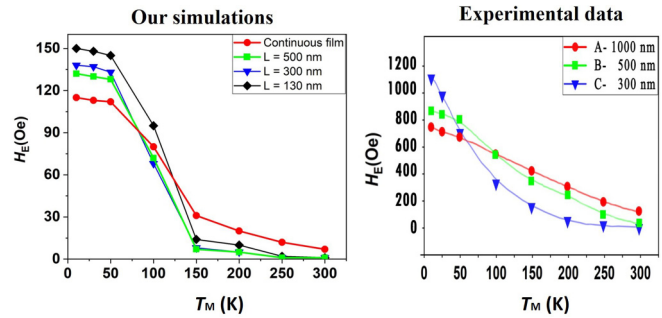

FIG. 8. Simulated temperature dependence of $|H_E|$ for NiFe/IrMn bilayers ($t_{IrMn} = 8$ nm) for (a) various nanodot sizes and continuous film in comparison with experimental data [11] (b).

IV. CONCLUSIONS

In this paper, we investigated the effects of reducing lateral sizes in F/AF nanodots using a granular model and kinetic Monte Carlo simulations. Our granular model took into account less stable magnetic grains at the F/AF interface due to atomic diffusions, stacking faults, etc. In the case of nanodots, additional less stable grains at the edges in the AF layer, due to the nanofabrication are considered. Our results demonstrated the crucial impact of the coupling between F grains. We evidenced that two different mechanisms of the F layer reversal can occur. An average-coupling behavior occurs with no variability from one nanodot to another when j_F is weak enough, corresponding to a reversal mechanism relying on several nucleation centers at any location within the film. In contrast, a j_F dependent behavior with unwanted [21] high variability from one nanodot to another takes place when j_F increases, corresponding to a reversal mechanism highly dependent on a single nucleation center at one corner of the nanodot and subsequent domain wall propagation. Our model also robustly accounts for several features experimentally observed in exchange-biased nanodots after several nontrivial experimental procedures are used to set the EB field by using only a single set of parameters.

ACKNOWLEDGMENTS

This project is funded by the Région Normandie and the European Union. Europe invests in Normandy with the European Regional Developement Fund (ERDF) - MAGMA project. The authors acknowledge the Centre Régional Informatique et d'Applications Numériques de Normandie (CRIANN) where simulations were performed as Project No. 2010006. We also thank Ahmed Albaalbaky for critical reading of the manuscript.

[1] W. H. Meiklejohn and C. P. Bean, Phys. Rev. **102**, 1413 (1956).
[2] W. H. Meiklejohn and C. P. Bean, Phys. Rev. **105**, 904 (1957).
[3] J. Noguès and I. K. Schuller, J. Magn. Magn. Mater. **192**, 203 (1999).
[4] A. E. Berkowitz and K. Takano, J. Magn. Magn. Mater. **200**, 552 (1999).
[5] I. L. Prejbeanu, M. Kerekes, R. C. Sousa, H. Sibuet, O. Redon, B. Dieny, and J. P. Nozieres, J. Phys.: Condens. Matter **19**, 165218 (2007).
[6] V. Baltz, A. Manchon, M. Tsoi, T. Moriyama, T. Ono, and Y. Tserkovnyak, Rev. Mod. Phys. **90**, 015005 (2018).
[7] C. Chappert, A. Fert, and F. N. Van Dau, Nat. Mater. **6**, 813 (2007).
[8] J. Noguès, J. Sort, V. Langlais, V. Skumryev, S. Surinach, J. S. Munoz, M. D. Baro, and I. K. Schuller, Phys. Rep. **422**, 65 (2005).
[9] V. Baltz, J. Sort, S. Landis, B. Rodmacq, and B. Dieny, Phys. Rev. Lett. **94**, 117201 (2005).
[10] V. Baltz, J. Sort, B. Rodmacq, B. Dieny, and S. Landis, Phys. Rev. B **72**, 104419 (2005).
[11] F. Spizzo, E. Bonfiglioli, M. Tamisari, A. Gerardino, G. Barucca, A. Notargiacomo, F. Chinni, and L. Del Bianco, Phys. Rev. B **91**, 064410 (2015).
[12] I. Sasaki, R. Nakatani, K. Ishimoto, Y. Endo, Y. Shiratsuchi, Y. Kawamura, and M. Yamamoto, J. Magn. Magn. Mater. **310**, 2677 (2007).
[13] Y. Shen, Y. Wu, H. Xie, K. Li, J. Qiu, and Z. Guo, J. Appl. Phys. **91**, 8001 (2002).
[14] G. Vinai, G. Gaudin, J. Moritz, J. Vogel, I. L. Prejbeanu, and B. Dieny, J. Phys. D: Appl. Phys. **47**, 195302 (2014).
[15] S. Laureti, S. Y. Suck, H. Haas, E. Prestat, O. Bourgeois, and D. Givord, Phys. Rev. Lett. **108**, 077205 (2012).
[16] V. Baltz, G. Gaudin, P. Somani, and B. Dieny, Appl. Phys. Lett. **96**, 262505 (2010).
[17] G. Garcia, M. Kiwi, J. Mejia-Lopez, and R. Ramirez, J. Magn. Magn. Mater. **322**, 3329 (2010).
[18] G. Vallejo-Fernandez and J. N. Chapmam, Appl. Phys. Lett. **94**, 262508 (2009).
[19] A. P. Malozemoff, Phys. Rev. B **35**, 3679 (1987).
[20] M. P. Proenca, J. Ventura, C. T. Sousa, M. Vazquez, and J. P. Araujo, Phys. Rev. B **87**, 134404 (2013).
[21] K. Akmaldinov, L. Frangou, C. Ducruet, C. Portemont, J. Pereira, I. Joumard, B. Dieny, J. Alvarez-Hérault, and V. Baltz, IEEE Magn. Lett. **6**, 3000404 (2015).
[22] G. Lhoutellier, D. Ledue, R. Patte, F. Barbe, B. Dieny, and V. Baltz, J. Phys. D: Appl. Phys. **48**, 115001 (2015).
[23] G. Lhoutellier, D. Ledue, R. Patte, and V. Baltz, J. Appl. Phys. **120**, 193902 (2016).
[24] R. Quey, P. R. Dawson, and F. Barbe, Comput. Methods Appl. Mech. Eng. **200**, 1729 (2011).
[25] E. Fulcomer and S. H. Charap, J. Appl. Phys. **43**, 4190 (1972).
[26] D. Choo, R. W. Chantrell, R. Lamberton, A. Johnston, and K. O'Grady, J. Appl. Phys. **101**, 09E521 (2007).
[27] B. Craig, R. Lamberton, A. Johnston, U. Nowak, R. W. Chantrell, and K. O'Grady, J. Appl. Phys. **103**, 07C102 (2008).
[28] M. D. Stiles and R. D. McMichael, Phys. Rev. B **60**, 12950 (1999).
[29] G. Vallejo-Fernandez, L. E. Fernandez-Outon, and K. O'Grady, Appl. Phys. Lett. **91**, 212503 (2007).
[30] D. Ledue, A. Maitre, F. Barbe, and L. Lechevallier, J. Magn. Magn. Mater. **372**, 134 (2014).
[31] L. Lechevallier, A. Zarefy, R. Lardé, H. Chiron, J. M. Le Breton, V. Baltz, B. Rodmacq, and B. Dieny, Phys. Rev. B **79**, 174434 (2009).
[32] L. Lechevallier, A. Zarefy, F. Letellier, R. Lardé, D. Blavette, J. M. Le Breton, V. Baltz, B. Rodmacq, and B. Dieny, J. Appl. Phys. **112**, 043904 (2012).
[33] K. Akmaldinov, S. Auret, I. Dieny, and V. Baltz Appl. Phys. Lett. **103**, 042415 (2013).
[34] D. W. Heermann, *Computer Simulation Methods in Theoretical Physics*, 2nd ed. (Springer, Berlin, 1990).
[35] K. Binder and D. W. Heermann, *Monte Carlo Simulation in Statistical Physics*, 2nd ed. (Springer, Berlin, 1990).
[36] S. Soeya, T. Imagawa, K. Mitsuoka, and S. Narishige, J. Appl. Phys. **76**, 5356 (1994).